Dendrite suppression in fast-charging high-energy metal-ion batteries: a Bayesian optimization approach

Hamed Taghavian, Viktor Vanoppen, Erik Berg, Peter Broqvist, Jens Sjölund

***Abstract*—Metal anodes provide the highest possible energy density in batteries. However, challenges associated with electrode/electrolyte interface side reactions and dendrite growth remain unsolved, especially under fast-charging conditions. In this paper, we consider a phase-field model of electrodeposition and optimize its parameters for suppressing dendrite growth and accelerating charging speed under constant voltage. We identify interfacial mobility as a key parameter, which should be maximized to inhibit dendrites without compromising the charging speed. The proposed approach provides a versatile tool for designing battery cells by optimizing an arbitrary objective function using an arbitrary set of parameters. This approach is based on Bayesian optimization and explores the parameters space with a high sample efficiency and a low computation complexity. The results are verified using extended simulations of dendrite evolution in charging half cells with lithium-metal anodes.**

I. INTRODUCTION

A. Background

Metal plating is the holy grail of rechargeable batteries, providing cells with the highest possible energy density. However, dendrite formation hinders the widespread use of these batteries, reduces their lifespan, and poses safety risks. Controlling dendrite growth by optimizing the batteries' chemical parameters is essential to address these challenges. Performing this optimization through real-world experiments is not only exceedingly time-consuming but also restricted by the challenges of precisely controlling the chemical parameters. Meanwhile, analytical expressions are too simplistic to capture the complex multi-scale nature of dendrite formation. Simulations, in particular ones based on phase-field models, strike a middle ground: offering a tractable yet physically realistic approach to a fundamental understanding of dendrite evolution in battery cells. These models have been proven useful in understanding the influence of several different parameters of batteries on dendrite growth. For example, phase-field models have shown that dendrite formation is inhibited when the applied voltage and exchange current density are low [1], the interface thickness is large [2], the separator has a small pore size [3] and there is high external pressure on the anode [4]. Phase-field models have also been used to describe the more nuanced effects of anisotropic strength and temperature on dendrite growth [5], [6].

Understanding the relation between different battery parameters and dendrite growth in phase-field models often relies on a complete simulation of dendrite evolution, by solving a system of nonlinear partial differential equations using the finite element method. While this approach is useful for investigating the effects of a single parameter on dendrite growth, it does not scale well with the number of influencing parameters. A significant amount of time and computational resources are needed to investigate the simultaneous effects of several parameters on dendrite growth. As there is a large number of parameters in phase-field models with an unknown effect on dendrites, a systematic approach is required to find the optimal set of parameters that inhibits dendrite growth. Furthermore, it is observed that minimizing only dendrite growth is a restrictive design objective that can lead to conservative solutions, which in extreme cases, leads to trivial solutions that stop charging completely. Therefore, when designing practical batteries, it is also important to consider charging speed which is often at odds with dendrite inhibition [7], [8].

B. Contributions

We present a scalable approach for exploration and optimization in the multi-dimensional parameter space of phase-field models. This approach provides a significant freedom of design through the choice of objective function. In particular, we demonstrate how additional design objectives, such as fast charging, can be incorporated alongside dendrite inhibition to obtain a more balanced solution. This versatility simplifies the battery design process, by replacing manual trial and error based on lengthy simulations or costly experiments.

1) Methodology: Our approach is based on Bayesian optimization, a machine-learning tool for optimization of black-box functions. We use this tool to find the optimal parameters of a battery cell that maximize an objective function, which is defined based on the electrode/electrolyte interface evolution of the battery cell during an electrodeposition process. This approach explores the parameters space more efficiently, using much fewer trials than an exhaustive search [9, §1]. By considering fast charging and dendrite suppression in the objective function, we obtain simple design rules, which reduce dendrite growth or increase the charging speed under a constant voltage, by tuning a few chemical parameters.

Our numerical simulations suggest that the interface evolution in a short time interval can provide reliable information on dendrite formation in prolonged charging sessions in some cases. Therefore, by shortening the observation interval and using the onset of dendrite formation, we further reduce the computational effort used in this framework. Moreover, we localize the phase-field equations in both space and time to gain more insight into how each parameter contributes to dendrite growth and charging speed. This localization reduces the system of partial differential equations in a phase-field model to a two-point boundary value problem in a small area of space and time. Using this reduced model, we define a few descriptors for the shapes of the electric and chemical potential fields and the deposition rate variations along the electrode/electrolyte interface. These descriptors, though approximate, can reveal the influence of certain parameters on the electrodeposition process without simulating the dendrite evolution even for a short amount of time. Therefore, by identifying and quantifying key descriptors that govern dendrite growth and charging speed, the complexity of the problem and the required computational efforts can be reduced which facilitates the systematic design of improved battery systems [10].

C. Organization

This paper is organized as follows. Section II briefly introduces the phase-field model we investigate. Then we construct a flexible design framework based on Bayesian optimization in Section III, which we use to optimize the parameters of the phase-field model with respect to dendrite growth and charging speed. As a result, we obtain simple rules that predict the influence of several parameters on the charging session in Section IV. These results are discussed in Section V, where we give further insight by localizing the phase-field model and evaluating a few descriptors associated with the shapes of electric and chemical potential fields and the electrodeposition rate variations along the electrode/electrolyte interface. Conclusive remarks are provided in Section VI.

II. Phase-field equations

Phase-field equations provide a unique way to study the morphological evolution of electrodeposited metals during charging processes, without needing to track the interface evolution. This is realized by using a "soft" parameter $\zeta \in [0,1]$ for describing phases, which is $\zeta = 1$ for the pure solid phase (electrode) and $\zeta = 0$ in the pure liquid phase (electrolyte). In this work, we are interested in the grand potential-based phase-field model provided by Hong and Viswanathan in [11], which describes the relation between the phase parameter ζ, chemical potential μ and electric potential ϕ in charging half cells, using the following system of partial differential equations:

$$\partial_t \zeta = -L_\sigma\big(g' - k\nabla^2\zeta\big) - L_\eta q \tag{1}$$
$$\partial_\mu c\,\partial_t \mu = \nabla\,.\,p\,(\nabla\mu + nF\nabla\phi) - \partial_\zeta c\,\partial_t\zeta \tag{2}$$
$$\nabla\,.\,(\sigma\nabla\phi) = nFC_m^s\partial_t\zeta, \tag{3}$$

where

$$\begin{aligned} h(\zeta) &= \zeta^3(6\zeta^2 - 15\zeta + 10) \qquad (4)\\ g(\zeta) &= W\zeta^2(1-\zeta)^2\\ c^{l,s}(\mu) &= \exp\left(\frac{\mu-\epsilon^{l,s}}{RT}\right)\Big/\left(1+\exp\left(\frac{\mu-\epsilon^{l,s}}{RT}\right)\right)\\ c_{M^{n+}}(\zeta,\mu) &= c^l(\mu)(1-h(\zeta))\\ q(\zeta,\mu,\phi) &= h'(\zeta)\left(\exp\left(\frac{(1-\alpha)nF}{RT}(\phi-E^\theta)\right)\right.\\ &\quad\left.-\frac{c_{M^{n+}}(\zeta,\mu)}{c_0}\exp\left(-\frac{\alpha nF}{RT}(\phi-E^\theta)\right)\right)\\ p(\zeta,\mu) &= D^l(1-h(\zeta))c_{M^{n+}}(\zeta,\mu)/RT\\ c(\zeta,\mu) &= c^l(\mu)(1-h(\zeta)) + c^s(\mu)h(\zeta)C_m^s/C_m^l\\ \sigma(\zeta) &= \sigma^s h(\zeta) + \sigma_l(1-h(\zeta)). \end{aligned}$$

In (4), h is an interpolation function for a smooth diffuse interface and h' denotes its derivative, g is a double-well function describing the equilibrium states of solid and liquid phases, c^s and c^l are the molar ratios in the solid and liquid phases, $c_{M^{n+}}$ is the local ion molar ratio, q is the driving force, c is the total concentration, and σ is the effective conductivity. The constant parameters in this model are interfacial mobility L_σ, gradient energy coefficient k, reaction constant L_η, the valence of charge carriers n, Faraday constant F, site density of electrolyte C_m^l, site density of electrode C_m^s, barrier height W, gas constant R, temperature T, the chemical potential differences on the electrolyte (electrode) at initial equilibrium state ϵ^l (ϵ^s), the standard equilibrium half-cell potential E^θ, charge transfer coefficient α, diffusion coefficient of the ions M^{n+} in the electrolyte D^l, initial molar ratio of ions c_0, and finally, the conductivities of electrolyte and electrode σ^l and σ^s. For a detailed derivation of these equations and the definition of their parameters consult [11], [12].

This paper aims at finding the parameters that optimize the electrodeposition process modeled by the phase-field equations (1)-(3). Several of these parameters are interconnected. For example, conductivity σ^l and diffusivity D^l are related through the Nernst–Einstein equation, and interfacial mobility L_σ and reaction coefficient L_η are related via the Allen Cahn equation [13], [14]. We relax these constraints, by assuming the parameters of the phase-field model (1)-(3) can be chosen independently.

III. Bayesian optimization

In this section, we develop a framework to find parameters of the phase-field model (1)-(3) that maximize a user-defined objective function. This framework is based on Bayesian optimization and is used to minimize dendrite growth and maximize charging speed in Section IV.

Let $\partial^2 u = [u, \partial_x u, \partial_y u, \partial_{xx} u, \partial_{yy} u]$ denote the vector of spatial partial derivatives of the function $u(x, y, t)$ up to order two. The phase-field equations can be written as the following shorthand nonlinear system of partial differential equations in space (x, y) and time t:

$$\partial_t \zeta = f_1(\partial^2 \zeta, \mu, \phi;\, \theta) \tag{5}$$
$$\partial_t \mu = f_2(\partial^2 \zeta, \partial^2 \mu, \partial^2 \phi;\, \theta) \tag{6}$$
$$0 = f_3(\partial^2 \zeta, \mu, \partial^2 \phi;\, \theta), \tag{7}$$

where the independent variables are omitted for convenience, and θ is a vector of selected constant parameters related to the chemical properties of the battery. We are interested in finding the optimal parameters $\theta^\star \in \Theta$ that result in the optimal plating (in a sense defined by the objective function) after charging the battery under constant voltage from the given initial state

$$\begin{aligned} \zeta(x, y, 0) &= \zeta_0(x, y) \\ \mu(x, y, 0) &= \mu_0(x, y) \end{aligned} \tag{8}$$

up until $t = t_f$. The set Θ determines the admissible ranges for each parameter in θ to prune out solutions that are unreasonable or practically infeasible.

A. *Objective function*

There is a freedom to choose the objective function based on the design goals. Herein, we are interested in dendrite inhibition and fast charging. Therefore, we choose an objective function that combines two functions corresponding to these two objectives. These functions measure dendrites and the state of charge in a cell.

1) Dendrites: To minimize dendrite growth in a cell, one first needs to define a function that measures the extent of dendrites. Several different functions have been proposed for this purpose in the literature, such as the distance between the longest dendrite's tip and the deepest valley in the cell (the maximum height), the time it takes dendrites to reach the opposite electrode (short-circuit time), and the relative length of the path that follows the electrode surface from top to bottom (tortuosity) [6], [15]. In the present work, we use the following dendrite measure based on the order parameter ζ:

$$\begin{aligned} \rho(t;\, \theta) = &\max_{y \in [y_0, y_f]} \int_{x_0}^{x_f} \zeta(x, y, t) dx \\ &- \min_{y \in [y_0, y_f]} \int_{x_0}^{x_f} \zeta(x, y, t) dx. \end{aligned} \tag{9}$$

The dendrite function (9) generalizes the maximum height measure in [15] to soft phase orders. Namely, if the phase order ζ is crisp at time t, *i.e.*, when

$$\begin{aligned} \zeta(x, y, t) &= 1, \quad x \leq x_0(y, t) \\ \zeta(x, y, t) &= 0, \quad x > x_0(y, t), \end{aligned}$$

then definition (9) falls back to the maximum height measure in [15] and $\rho(t) = 0$ holds if and only if the surface of the electrode is flat.

Different dendrite functions were observed to yield similar results when studying dendrite growth during charging [6], [15]. Nevertheless, we have chosen function (9) for two main reasons. First, despite tortuosity, it better captures the needle-like dendrites that risk internal short circuits, a well-known cause of thermal run-away in batteries [16, §6.1.2.1]. Second, despite the short-circuit time, it can be computed using the current order parameter value with no need to simulate the charging process until short-circuit.

2) state of charge: To maximize the charging speed, we maximize the state of charge at the end of the charging session t_f. The state of charge at time t can be estimated by measuring the surface of the electrode relative to the total area of the cell as follows

$$S(t; \theta) = \frac{\int_{y_0}^{y_f} \int_{x_0}^{x_f} \zeta(x, y, t) dx dy}{2(x_f - x_0)(y_f - y_0)}, \tag{10}$$

where the denominator is the area of the cell (double the half-cell area).

Note that since the order parameter ζ evolves differently for different parameter values in (1)-(3), both ρ and S are functions of the selected parameters θ in (9) and (10). Therefore, to inhibit dendrite growth and accelerate charging speed, one may look for the optimal parameters $\theta^\star$ that maximize an averaged objective function as follows:

$$C(t, \theta) = -\lambda \rho(t; \theta) + (1 - \lambda) \bar{S}(t; \theta), \tag{11}$$

where we have scaled the state of charge as $\bar{S}(t; \theta) = 2(x_f - x_0) S(t; \theta)$ to make sure $\bar{S}(t; \theta)$ and $\rho(t; \theta)$ are within the same range

$$\bar{S}(t; \theta), \rho(t; \theta) \in [0, x_f - x_0].$$

In (11), $\lambda \in [0, 1]$ specifies the trade-off between the two objectives; To speed up charging, we can choose a smaller value for λ, while to inhibit dendrites we can increase λ.

B. Optimization problem

We consider the following optimization problem:

$$\begin{aligned} \underset{\theta\in\Theta}{\text{maximize}} \quad & C(t_f;\theta) \\ \text{subject to} \quad & \zeta, \mu, \phi \text{ satisfy (1)-(3).} \end{aligned} \tag{12}$$

Evaluating the objective function in (12) at a given point θ requires simulating the phase-field equations (1)-(3) for $t \in [0, t_f]$ to obtain $\zeta(x, y, t_f)$, which is plugged in (9) and (10) to compute the dendrite and state-of-charge functions. This process requires a significant amount of time and computation power. In addition, no explicit expression is known for the objective function in (12) and there is no efficient method available for estimating its gradient, rendering most traditional optimization paradigms inapplicable. Therefore, we consider the objective function (12) as a black box and use Bayesian optimization to solve the problem (12). The remarkable sample efficiency of Bayesian optimization further motivates this choice among other global optimization routines, because of the costliness of function evaluations in (12) [9, §1].

IV. Results

We apply the Bayesian optimization framework developed above to find the optimal parameters σ^s, σ^l, C_m^l, D^l, L_σ and L_η in a lithium-metal half cell. The feasible intervals used for these parameters are listed in Table III. These intervals are derived from perturbing the nominal values in [17] by a maximum of 50% and include the parameter values used in various studies with different electrodes and electrolytes [1], [5], [11], [12], [15], [18], [19], [20], [21]. The rest of the parameters in (1)-(3) are chosen according to [17]. To make the simulations more realistic, we use an electrode with an initially rough surface shown in Figure 1a, as no electrode has a perfectly flat surface in practice. This initial roughness of the electrode surface also makes dendrites grow faster, which can help to save computation power by choosing a smaller t_f in (12).

A. Minimizing dendrite growth

To only minimize dendrite growth, we choose $\lambda = 1$ in the objective function in (12). As a first experiment, we solve the optimization problem (12) with a short time horizon $t_f = 0.04$ (s) once for each parameter $\theta \in \mathbb{R}$ in Table III. The rest of the parameters are kept constant at the center of their intervals. All the parameters are found to be optimal at their extreme values as shown under the column $\lambda = 1$ of Table III. Hence, the results of this experiment can be summarized by a simple rule of thumb for tuning the battery parameters to inhibit dendrites as shown in Table I.

Parameter	Rule of thumb
Electronic conductivity of the solid phase σ^s	Increase
Ionic conductivity of the liquid phase σ^l	Decrease
Site density in electrolyte C_m^l	Decrease
Diffusion coefficient of ions M^{n+} in electrolyte D^l	Decrease
Interfacial mobility L_σ	Increase
Electrochemical reaction kinetic coefficient L_η	Decrease

TABLE I: Guideline on choosing the parameter values for *minimal dendrite growth* in the lithium-metal half cell considered in Section IV.

Parameter	Rule of thumb
Electronic conductivity of the solid phase σ^s	Decrease
Ionic conductivity of the liquid phase σ^l	Increase
Site density in electrolyte C_m^l	Increase
Diffusion coefficient of ions M^{n+} in electrolyte D^l	Increase
Interfacial mobility L_σ	Increase
Electrochemical reaction kinetic coefficient L_η	Increase

TABLE II: Guideline on choosing the parameter values for *maximum charging speed* in the lithium-metal half cell considered in Section IV.

In the second experiment, we increase the horizon length in the first experiment by 2.5 times, *i.e.*, $t_f = 0.1$ (s) and optimize all the first four parameters in Table III simultaneously ($\theta \in \mathbb{R}^4$). The results of this experiment coincide with those of the first experiment perfectly. This suggests that the optimal solution to (12) is not sensitive to t_f. Therefore, one may choose a smaller value for t_f to make the function evaluation steps less costly and reduce the computation burden in solving the optimization problem (12) significantly.

To validate the results in Table I, we consider charging a half cell at constant voltage -0.45 (v) using two different values for the parameters σ^s, σ^l, D^l, C_m^l and compare the results in Figure 1. First, these parameters were chosen based on the guidelines of Table I (with the exact values given in column $\lambda = 1$ of Table III). No dendrites grow in this experiment (see Figure 1b). However, when these parameters are chosen as the mid-points of their respective intervals in Table III, dendrites grow (Figure 1a).

This observation confirms the results of Table I. However, it also has two important indications. First, it suggests that the parameters that minimize dendrite growth within a short time interval $t_f = 0.04$ (s) can also inhibit dendrites further in the future $t_f = 60$ (s). Second, it shows dendrite inhibition can be at odds with fast charging. Because the amount of charge delivered

Parameter	notation	unit	value range	$\lambda = 1$	$\lambda = 0$
Electronic conductivity of the solid phase	σ^s	[S/m]	$10^6 \times [0.5, 1.5]$	1.5×10^6	0.5×10^6
Ionic conductivity of the liquid phase	σ^l	[S/m]	$[0.5950, 1.7850]$	0.5950	0.6866
Site density in electrolyte	C_m^l	[mol/m^3]	$10^4[0.9261, 2.7782]$	0.9261×10^4	2.7782×10^4
Diffusion coefficient of ions M^{n+} in electrolyte	D^l	[m^2/s]	$10^{-9}[0.1590, 0.4769]$	0.1590×10^{-9}	0.4769×10^{-9}
Interfacial mobility	L_σ	[m^3/Js]	$10^{-5}[0.1250, 0.3750]$	0.3750×10^{-5}	0.3750×10^{-5}
Electrochemical reaction kinetic coefficient	L_η	[s^{-1}]	$[0.0005, 0.0015]$	0.0005	0.0015

TABLE III: The optimal parameters that maximize the objective function (11) with different values of λ found by Bayesian optimization. The parameters in the column $\lambda = 0$ maximize the charging speed, while the parameters in the column $\lambda = 1$ inhibit dendrite growth.

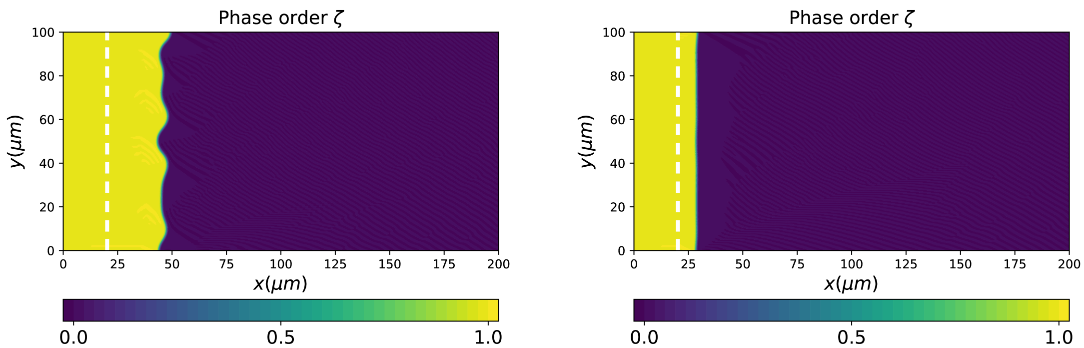

(a) The half cell with parameters chosen from [17] develops dendrites and reaches the state of charge 0.12 in 60 (s).

(b) The half cell with parameters chosen according to Table I forms no dendrites and reaches the state of charge 0.07 in 60 (s).

Fig. 1: Two half cells charged with the same constant voltage -0.45 (v) and the same amount of time 60 (s). The dashed line shows the initial interface at the beginning of the charging process.

in the two half cells during the same time interval of 60 (s) is strikingly different in Figure 1. The cell state of charge at the end of the charging session in Figure 1b is estimated to be 0.072, that is, around 37% less than that in Figure 1a. Therefore, choosing extreme values for dendrite inhibition can lead to conservative solutions that slows the charging process.

B. Maximizing charging speed

We choose $\lambda = 0$ in the objective function (11) to optimize the parameters for fast charging. Bayesian optimization was used to solve this optimization problem with $t_f = 0.04$ (s). The results are reported under the column $\lambda = 0$ in Table III and summarized as a simple rule in Table II. Again, all the parameters are found to be optimal at their extreme values, however, except interfacial mobility, on the opposite sides of their spectrums. This agrees with the observation in Figure 1 where fast charging and minimal dendrite growth are at odds.

C. Simultaneously minimizing dendrite growth and maximizing charging speed

One can settle for a middle ground between fast charging and dendrite inhibition by tuning the objective function in the optimization problem (12) using $\lambda \in (0, 1)$. By using a smaller λ, the parameters that speed up charging are favored, whereas a larger λ would lead to parameters that inhibit dendrite growth.

Nevertheless, a curious exception to the trade-off between the conflicting objectives of dendrite inhibition and fast charging is the interfacial mobility L_σ. This parameter should be maximized to achieve both fast charging and minimum dendrite growth, according to Tables I, II, and III.

To examine how this parameter affects the charging performance, we consider two half cells with different interfacial mobilities and otherwise equal parameters according to [17]. These half cells are charged with the constant voltage -0.45 (v) for 110 (s). We simulate the dendrite growth in both half cells and compare the results in Figure 2. As shown in Figure 2a, dendrites are only formed in the half cell with the smaller L_σ.

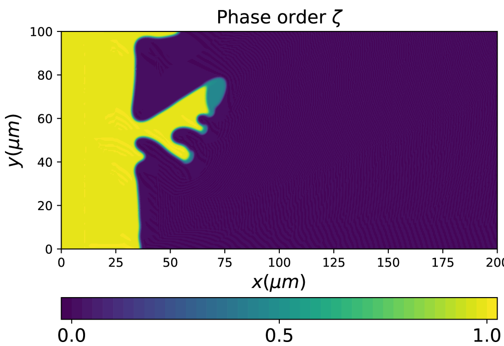

(a) The half cell with $L_\sigma = 0.4 \times 10^{-6}$ (m^3/Js) develops dendrites and reaches the state of charge 0.10 in 110 (s).

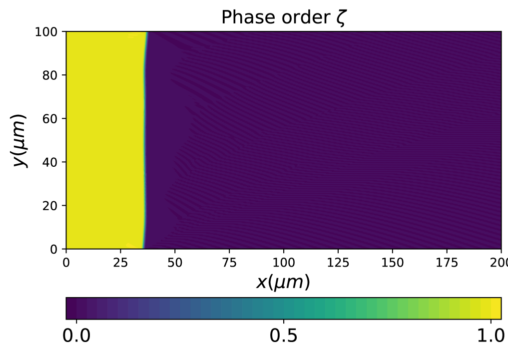

(b) The half cell with $L_\sigma = 8 \times 10^{-6}$ (m^3/Js) reaches the state of charge 0.09 in 110 (s) with no visible dendrites.

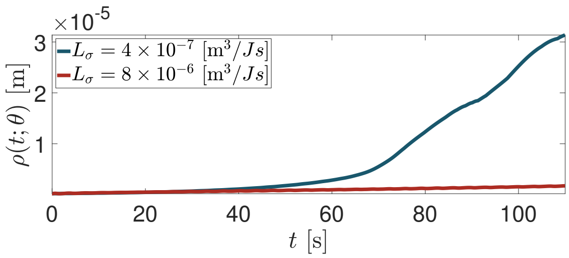

(c) The roughness of the electrode surface (9) over time.

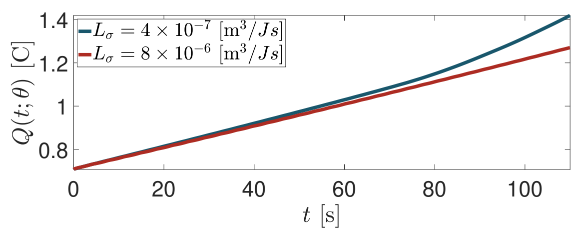

(d) The delivered charge (13) over time.

Fig. 2: Two half cells charged with the same constant voltage -0.45 (v) and the same amount of time 110 (s). The only different parameter between these two half cells is the interfacial mobility L_σ.

The roughness of the electrode surface (9) grows more rapidly in this half cell (see Figure 2c). Nevertheless, in both half cells, the electrode surface (excluding the dendrite) is approximately located at 35 (μm) on the horizontal axis, which indicates a similar charging speed between the two experiments (see Figures 2a and 2b).

An alternative way to compare the charging speeds between the two experiments is estimating the delivered electric charge in each half cell up to time t, by using the following function

$$Q(t;\,\theta) = nFC_m^s \int_{y_0}^{y_f} \int_{x_0}^{x_f} h\left(\zeta(x,y,t)\right) dxdy. \quad (13)$$

The above function grows slightly faster in the half cell with the smaller L_σ. However, the charge delivered in the other half cell is not far behind, growing almost linearly (see Figure 2d). Note that both functions (10) and (13) are based on the total area occupied by the solid phase, including the dendrite. At the end of the experiment, the state of charge (10) in Figure 2b is 10.6% less than the state of charge in Figure 2a. In comparison, recall that when dendrites were inhibited by tuning the parameters σ^s, σ^l, D^l, C_m^l instead of L_σ, the state of charge in Figure 1b was 37% less than the state of charge in Figure 1a. Therefore, we conclude that increasing L_σ inhibits dendrites more effectively with much less impact on the charging speed.

V. Discussion

In Section IV, we identified the influence of different cell parameters on the speed and dendrite formation in a charging process. In this section, we discuss *how* these parameters influence the charging session the way they do. To simplify our discussions, we also quantify several key descriptors for the local behavior of the electrode/electrolyte interface during the electrodeposition process. Analyzing these descriptors instead of the full model (1)-(3) helps to understand the mechanism by which different parameters affect the charging process.

A. *Local behavior of the interface*

We begin with approximating the phase-field model (1)-(3) across the phase transition interface in an infinitesimal time interval, a process we call *localization*. By restricting space and time in this way, the system of partial differential equations is replaced by an ordinary differential equation around the phase transition interface. This simplified local model provides four descriptors (Table IV) for the shapes of the electric and chemical potential fields and the deposition rate variations along the electrode surface. These descriptors are functions of the battery parameters and provide valuable information on how each parameter contributes to dendrite growth and charging speed.

1) Localization: Consider a half cell where the negative electrode made of M metal is located on the left and the electrolyte is on the right. During the charging process, the electrochemical potential governs the transport of M^{n+} ions through the electrolyte and their adsorption on the anode. Hence, to understand the effects of different battery parameters on electrodeposition and dendrite growth, we study their effects on the electric and chemical potentials. To simplify the process, we consider the phase-field equations (1)-(3) in a small box within the electrode/electrolyte interface where the phase order parameter varies from $\zeta = \zeta_0$ to $\zeta = \zeta_1$ (see Figure 3) where

$$0 < \zeta_0 < \zeta_1 < 1.$$

Such a local analysis is useful as the electrode/electrolyte interface is where most of the limiting processes occur in a charging cell [16, §1.5]. We assume that the level sets of ζ, μ and ϕ are parallel in this box and

$$\begin{aligned} \zeta &= \big(\tanh \beta(z - z_0) + 1\big)/2 \\ \mu &= \mu_s \zeta, \end{aligned} \tag{14}$$

where $z = y$ in case the surface normal inside the box is orthogonal to the charging direction (Figure 3a) and $z = x$ when it is parallel to it (Figure 3b). In (14), z_0 specifies the transition interface location, $\beta > 0$ determines the sharpness of phase transition, and $\mu_s < 0$ is the chemical potential limit in the solid phase. Functions (14) are a smooth approximation of step functions commonly used in the literature, including for representing order parameters and electric potentials [17]. Although assuming parallel level sets may look restrictive, it typically holds inside a small enough box on the tip and sides of grown dendrites (see for example [17]).

The above assumptions simplify the phase-field equations significantly. In particular, substituting (14) and (1) in the Poisson equation (3) results in a second-order *ordinary* differential equation in ϕ, which after changing the independent variable from z to ζ, takes the form

$$a_2(\zeta)\phi'' + a_1(\zeta)\phi' = a_0(\zeta, \phi), \tag{15}$$

with the two-point boundary conditions

$$\phi(\zeta_0) = \phi_0,\ \phi(\zeta_1) = \phi_1 \tag{16}$$

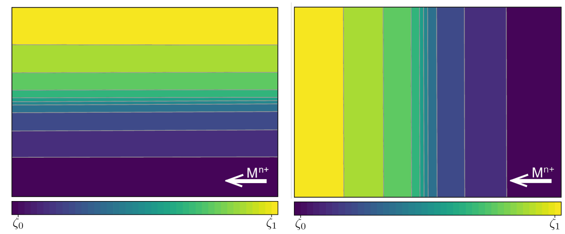

(a) $z = y$. (b) $z = x$.

Fig. 3: Level sets of the order parameter ζ in a small box around the electrode/electrolyte transition zone ($\zeta_0 < \zeta_1$). The white arrow indicates the charging direction.

and coefficient functions

$$\begin{aligned} a_2(\zeta) &= \sigma\zeta(1-\zeta) \\ a_1(\zeta) &= 30(\sigma^s - \sigma^l)\zeta^3(1-\zeta)^3 - \sigma(2\zeta - 1) \\ a_0(\zeta, \phi) &= \frac{nFC_m^s}{2\beta^2}\big(L\sigma(2\zeta-1)(W - 2\beta^2 k) \\ &\quad - L_\eta q(\zeta, \mu_s\zeta, \phi)/2\zeta(1-\zeta)\big). \end{aligned} \tag{17}$$

Note that the phase-field equations are symmetrical in the coordinates x and y (except the initial and boundary conditions). Therefore, the above equations are valid for both boxes in Figure 3 independent of the choice $z \in \{x, y\}$.

Equations (15)-(17) specify a two-point boundary value problem that can be solved by, *e.g.*, collocation and shooting methods to obtain $\phi = \phi(\zeta)$. This solution determines the electric potential inside the box and, along with ζ and μ from (14), can be substituted in (2) and (1) to obtain the chemical potential derivative $\partial_t\mu$ and the electrodeposition rate $\partial_t\zeta$ within the transition zone $\zeta \in (\zeta_0, \zeta_1)$. We use ϕ, $\partial_t\mu$ and $\partial_t\zeta$ to define descriptors.

2) Electric potential: The electrodeposition process curves the electric potential level-sets forward. This phenomenon, observed in numerous studies on different phase-field models (see, *e.g.*, [1], [12], [22]), has been acknowledged as a contributing factor to further dendrite growth [11], [18], [23], [24]. Figure 4 demonstrates this effect by showing a half cell with a grown dendrite (black curve) being charged in a curved electric field (Figure 4a) versus a straight electric field (Figure 4b). As the electric potential level sets are orthogonal to the electric field, the cations M^{n+} are forced toward the dendrite in the curved field, resulting in its further growth (Figure 4a). In contrast, in an ideal case where the electric potential level sets are straight, the dendrite cannot grow larger, because the electric force direction is unchanged throughout the half cell, and thereby, the ions M^{n+} tend to move straight toward the electrode

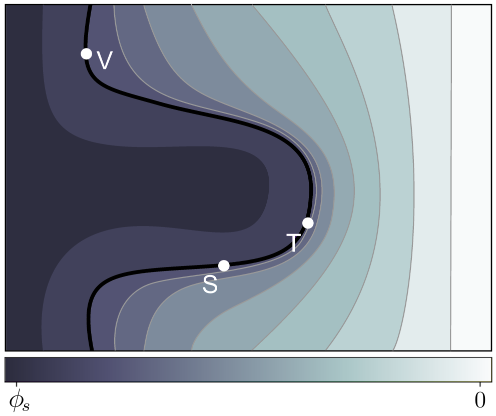

(a) Curved electric potential level sets promote dendrite growth.

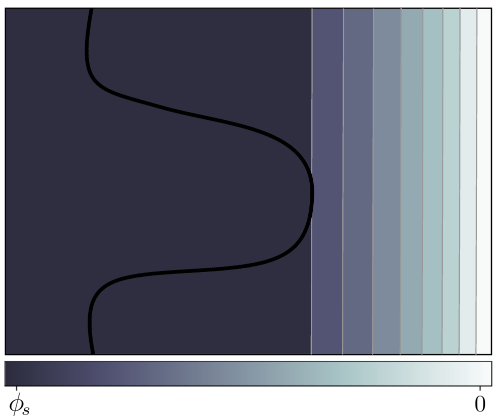

(b) Linear electric potential level sets inhibit dendrite growth

Fig. 4: The electric potential level sets in a charging half cell, where the anode is on the left and the electrolyte is on the right ($\phi_s < 0$). The black curve shows the electrode/electrolyte interface, which is *sharp* unlike in Figure 3.

(see Figure 4b). Therefore, a less curved electric field can inhibit dendrite growth.

Whether the electric field in Figure 4 is curved or not can be detected by observing the electric potential inside a small box within the interface, similar to the one shown in Figure 3, at either of the points S (side), T (tip), or V (valley). In the curved field (Figure 4a), the electric potential changes more rapidly on the liquid side compared to the solid side. However, in the straight field (Figure 4b), the electric potential changes uniformly across the interface in both boxes. Let $\phi(\zeta)$ be the solution to (15) and

$$d^\phi := \phi\left(\frac{\zeta_0 + \zeta_1}{2}\right) \tag{18}$$

denote the electric potential at the interface center. Since

$$\begin{aligned} d^\phi &= \phi_0 + \int_{\zeta_0}^{(\zeta_0+\zeta_1)/2} \phi'(\zeta) d\zeta \\ &= \phi_1 - \int_{(\zeta_0+\zeta_1)/2}^{\zeta_1} \phi'(\zeta) d\zeta, \end{aligned}$$

assuming a decreasing electric potential across the interface and the same boundary conditions (16), the cell with a smaller d^ϕ has a larger total absolute change in ϕ on the liquid side of the interface ($\zeta \in [\zeta_0, (\zeta_0+\zeta_1)/2]$) and a smaller one on the solid side ($\zeta \in [(\zeta_0+\zeta_1)/2, \zeta_1]$). Therefore, a more severe dendrite growth is expected when d^ϕ is small. Straightness of the electric field is not the only factor that suppresses dendrite formation. A more common way to inhibit dendrites is through the chemical potential build up near the electrode surface, which is introduced next.

3) Chemical potential: Diffusion of ions through the electrolyte often occurs at a much slower rate than their reduction and adsorption on the electrode surface. This condition promotes dendrite growth by consuming the ions M^{n+} as soon as they reach the electrode surface. Slowing the adsorption or speeding up the diffusion process can help avoid this condition by saturating the reaction spots with an accumulation of ions near the electrode surface [6]. This accumulation of ions would eventually reverse the concentration gradient inside the cell and inhibit dendrite growth. The reason is that the ions are forced towards regions with a lower concentration which counteracts the electric force that promotes dendrite growth in Figure 4a.

Figure 5 shows what the concentration field looks like when a half cell is charged in these two scenarios. The former case is shown in Figure 5a, where the local concentration decreases when moving from the bulk electrolyte toward the electrode. In contrast, in the latter case shown in Figure 5b, the local concentration near the electrode is higher than that in the bulk electrolyte. Note that there is a monotonic relation between concentration $c_{M^{n+}} = c^l(\mu)$ and chemical potential μ given a fixed phase order (see (4)). Hence, the accumulation of ions in Figure 5b manifests as a chemical potential build up close to the electrode surface. This form of dendrite inhibition only occurs in the long term when the electrode surface is saturated, and as such, it is hard to detect in a local approximate model.

Nevertheless, the local model of Section V-A1 can detect the chemical potential growth rate within the electrode/electrolyte interface, which at high levels, implies accelerated charging. To examine this, one may solve (15) for ϕ and substitute the solution in (2) to obtain the chemical potential time-derivatives inside the box. Then

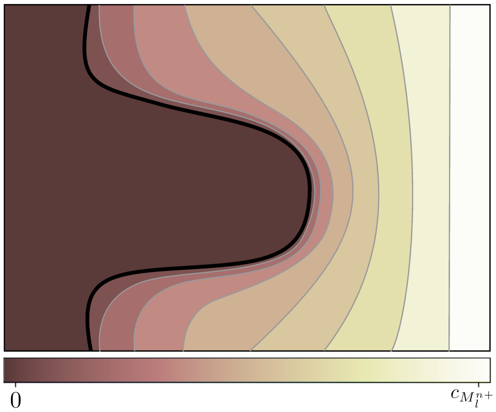

(a) A decreasing concentration toward the electrode promotes dendrite growth. In this case, the chemical potential is *lower* close to the interface than the bulk electrolyte.

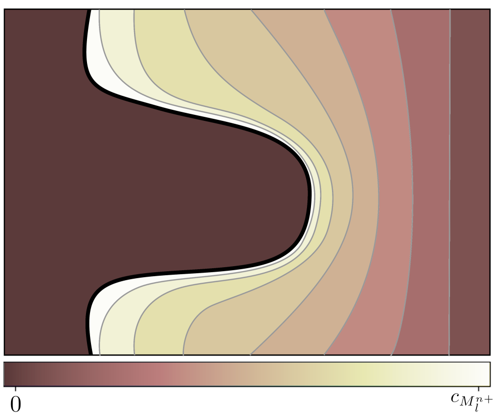

(b) An increasing concentration toward the electrode inhibits dendrite growth. In this case, the chemical potential is *higher* close to the interface than the bulk electrolyte.

Fig. 5: Ion concentration (molar ratio) level-sets in a charging half cell, where the anode is on the left and the electrolyte is on the right ($0 < c_{M_l^{n+}}$). The black curve shows the electrode/electrolyte interface, which is *sharp* unlike in Figure 3.

we define the descriptor

$$d^{\mu} := \frac{1}{\zeta_1 - \zeta_0} \int_{\zeta_0}^{\zeta_1} \partial_t \mu d\zeta, \tag{19}$$

which measures the average growth rate of chemical potential within the interface. A larger d^{μ} indicates a faster plating within the interface and therefore, a faster charging process.

4) Deposition rate: Electrodeposition mainly occurs within the interface, though at different rates, depending on the region. Typically, a valley region (point V in Figure 4a) grows more slowly than a tip region (point T in Figure 4a), leading to dendrite growth on the electrode. A similar deposition rate at the tip and valley regions indicates that dendrites do not grow larger.

Notation	Associated with	Effect
d^{ϕ}	Linearity of the electric field	Dendrite inhibition
d^{μ}	Chemical potential build up	Fast charging
$d^{\zeta}_{\text{val}} - d^{\zeta}_{\text{tip}}$	Deposition uniformity	Dendrite inhibition
$d^{\zeta}_{\text{val}} + d^{\zeta}_{\text{tip}}$	Average deposition rate	Fast charging

TABLE IV: Descriptors suggestive of fast charging and dendrite growth. A larger value of these descriptors implies the effects described in the last column.

It is possible to evaluate the electrodeposition rates in different regions by using the local model developed in Section V-A1. As can be seen in Figure 4, the electric potential tends to vary less across the interface in the valley regions (*e.g.*, point V) compared to the tip regions (*e.g.*, point T). This phenomenon which is also observed in [3], [18] makes it possible to distinguish a valley from a tip region by the different boundary conditions (16). Therefore to obtain the electric potential in these two regions, equation (15) is solved for ϕ using two different boundary conditions that satisfy

$$\phi_1^{\text{tip}} < \phi_1^{\text{val}} < \phi_0^{\text{val}} < \phi_0^{\text{tip}}$$

Then the solutions are substituted for ϕ in (1) to give the electrodeposition rates in the tip and valley regions. Let us denote the deposition rates at the tip and valley regions by $\partial_t \zeta^{\text{tip}}$ and $\partial_t \zeta^{\text{val}}$ respectively and define the descriptors

$$d^{\zeta}_{\text{val}} := \frac{1}{\zeta_1 - \zeta_0} \int_{\zeta_0}^{\zeta_1} \partial_t \zeta^{\text{val}} d\zeta,$$

$$d^{\zeta}_{\text{tip}} := \frac{1}{\zeta_1 - \zeta_0} \int_{\zeta_0}^{\zeta_1} \partial_t \zeta^{\text{tip}} d\zeta.$$

Dendrites are expected to grow slower in a cell where the quantity $d^{\zeta}_{\text{val}} - d^{\zeta}_{\text{tip}}$ is large while the cell is expected to charge faster when the average deposition rate in the valley and tip regions, *i.e.*, the quantity $d^{\zeta}_{\text{val}} + d^{\zeta}_{\text{tip}}$ is large.

B. Influencing parameters

We defined four different descriptors associated with dendrite growth and charging speed that are summarized in Table IV. We use these descriptors along with the results of Section IV to elaborate on the influence of different parameters on the charging process in this section. We consider a lithium-metal half-cell battery with the parameters reported in [11]. To calculate the descriptors in Table IV we choose $\zeta_0 = 0.3$, $\zeta_1 = 0.7$, $\beta = 10$, $\mu_s = -10$ for the local approximation (14).[1]

[1]The chosen values are not definitive. Alternative values could be used for this experiment.

1) Conductivity: According to Table III, a larger electronic conductivity of the electrode σ^s can inhibit dendrite growth. This inhibition of dendrites is a consequence of a low electric field curvature. To see this, we note that the conductivities of the electrode and electrolyte are the only parameters that exclusively shape the electric potential via the Poisson equation (3). In particular, to reveal the effect of electrode conductivity on the electric field curvature we compute the descriptor d^ϕ in (18) for three different values of σ^s. It is observed that a larger conductivity of the electrode results in a larger d^ϕ, and thereby, a more straight electric field. Figure 6 shows this effect by plotting the electric field across the interface $\zeta \in [\zeta_0, \zeta_1]$. These results show no trade-off between dendrite inhibition and most other desirable performance objectives in batteries when choosing electrode conductivity σ^s. For example, a large σ^s is also desirable to achieve a good rate performance, etc. [25], [26].

In contrast, a smaller ionic conductivity of the electrolyte σ^l can inhibit dendrite growth, according to Table III. This kind of dendrite inhibition comes, however, with a trade-off, as a high ionic conductivity of the electrolyte is desirable for the cell overall performance [16, §1.5.4]. The suppressive effect of lower ionic conductivity of the electrolyte is supported by findings from Rehnlund et al. reporting that reducing lithium salt concentration decreases ionic conductivity and mitigates dendrite formation by favoring two-dimensional lithium deposition under diffusion-controlled conditions [27].

The results in Table III also state that the half cell is charged faster when the ionic conductivity of electrolyte is high. This is of course expected, as the half-cell resistance is dominated by the electrolyte resistance and when this resistance is low, the charging current is high under a constant voltage by the Ohm's rule.

There are several ways to change conductivities in a battery cell. One may change the electrode conductivity σ^s, by *e.g.*, tuning the metal composition (alloying) and the operating temperature. It is possible to change the electrolyte conductivity σ^l, by *e.g.*, changing the viscosity, the used solvent, the salt concentration, or the temperature [16, §1.5.4].

2) Diffusivity: The only parameters that exclusively influence the chemical potential via the diffusion equation (2) are the diffusion coefficient D^l and the site density of electrolyte C^l_m. To study the effects of the diffusion coefficient on chemical potential, we calculate d^μ for different values of D^l by solving the equation (15) and substituting its solution in (2) to obtain the chemical potential derivatives as shown in Figure 7. It is observed that a larger D^l results in a larger d^μ and therefore, in a chemical potential build up near the electrode surface. This results in faster charging confirming the results of Table III.

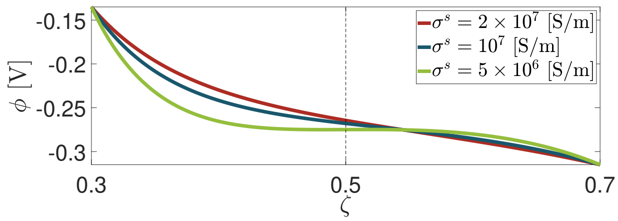

Fig. 6: A larger electrode conductivity σ^s yields a more straight electric field across the phase transition zone, and therefore, less dendrite growth.

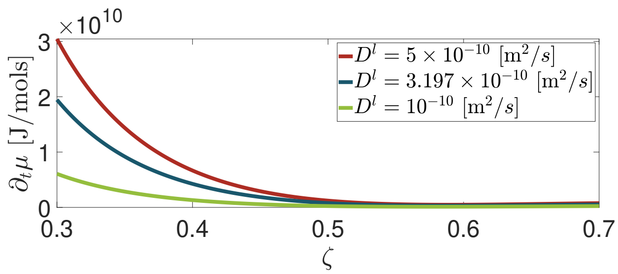

Fig. 7: A larger D^l yields a higher chemical potential growth rate on average.

Table III also states that a smaller diffusion coefficient results in less dendrite growth, which is contradictory to most available guidelines that suggest inhibiting dendrites by reaction-limited regimes [6], [28]. However, a short-term dendrite inhibition as in Table III is a consequence of slower ion transport, rather than an accumulation of ions explained in Section V-A3 [29]. In contrast, dendrite inhibition in [6], [28] is the result of ion accumulation and is only achieved after saturating the interface with ions and building up a reverse concentration gradient (see Figure 5b). An opposite trend holds before reaching this point, according to Table III. Similar to electrolyte conductivity, the diffusion coefficient D^l can also be changed in various ways, including changing the viscosity of the electrolyte.

3) Reaction constant and interfacial mobility: According to Table III, a lower electrochemical reaction kinetic constant L_η can inhibit dendrite growth. The reaction constant L_η has a direct relation with the exchange current density i_0 [30] and it is well-documented that a lower current density i_0 also inhibits dendrites [31], which confirms our results. A lower exchange current density can be achieved via anti-catalysis, *i.e.*, by tailoring specifically the electrode surface composition, *e.g.*, with adsorption of other metal cations.

Table III also shows that a lower reaction constant L_η slows down charging, which is again expected, due to the slower electrochemical reactions. In addition, a direct relation is observed between the descriptor d^{μ} and L_{η}, which confirms this result.

A high interfacial mobility can inhibit dendrite growth and accelerate charging, according to Table III. We leverage the descriptors d^{ζ}_{val} and d^{ζ}_{tip} to study this effect. For this purpose, we consider the differential equation (15) once with each of the following boundary conditions:

$$\phi(\zeta_0) = -0.1,\ \phi(\zeta_1) = -0.6, \qquad \text{tip region}$$
$$\phi(\zeta_0) = -0.3,\ \phi(\zeta_1) = -0.5, \qquad \text{valley region}$$

Equation (15) is solved for ϕ using different values of L_{σ}. The solution ϕ is then substituted in (1) to obtain the electrodeposition rates in the tip and valley regions. Figures 8a and 8b show the electrodeposition rate uniformity $d^{\zeta}_{\text{val}} - d^{\zeta}_{\text{tip}}$ and the average electrodeposition rate $d^{\zeta}_{\text{val}} + d^{\zeta}_{\text{tip}}$ along the electrode surface, respectively. Both these descriptors are increasing with L_{σ}, which confirms our results in Table III. This also agrees with the trend seen in the chemical potential growth rate in Figure 8c. However, an opposite trend is observed in d^{ϕ} (Figure 8d), which indicates that the dendrite inhibition achieved by increasing interfacial mobility is not caused by straightening the electric field. Rather, a high interfacial mobility facilitates the surface tension release, which results in a smoother electrode surface and therefore in less dendrite growth.

The above results also align with trends observed in the broader electroplating industry. In copper electroplating, for example, the control of deposition behavior is largely chemistry-driven, with additives playing a critical role. Suppressors, adsorb on the copper surface and selectively reduce the deposition rate in high-current-density regions like tips, effectively promoting uniform deposition by slowing plating in these areas. Accelerators, counteract the suppressor effect by increasing deposition rates in valley regions where suppressors are less adsorbed, ensuring a balanced deposition and reducing surface roughness. Levelers, acting as secondary suppressors, specifically target protrusions such as dendrite tips to minimize surface irregularities and ensure smoother plating. Together, these additives indirectly adjust L_{σ} and L_{η}, with suppressors and levelers mimicking the effects of high L_{σ} by reducing unevenness, while accelerators fine-tune deposition rates to prevent over-suppression [32]. Similar efforts have been made for lithium with different approaches aimed at improving the interfacial mobility of Li-ions on the surface of the electrode [33], [34], [35].

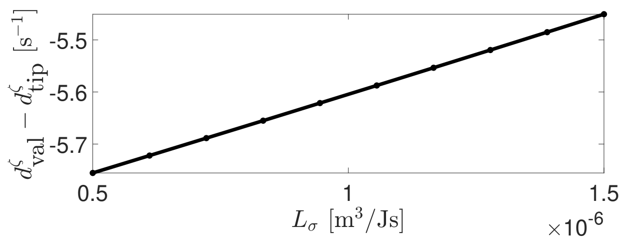

(a) High interfacial mobility yields a more uniform deposition rate along the electrode surface and hence, less dendrite growth.

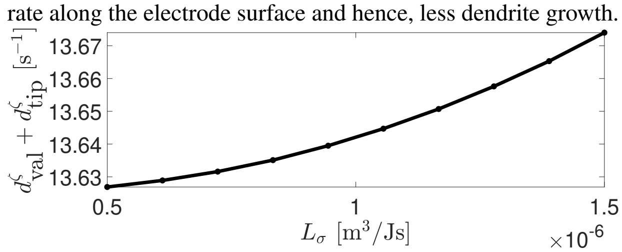

(b) High interfacial mobility yields a faster deposition on average and hence, a higher charging speed.

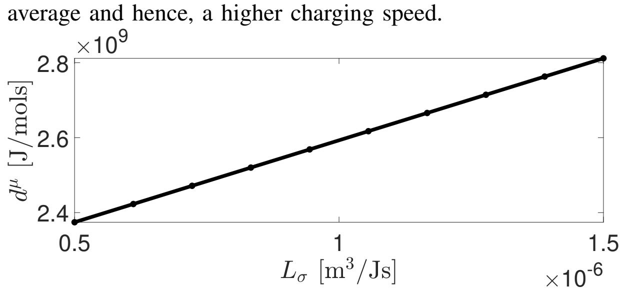

(c) High interfacial mobility accumulates ions within the interface and builds up the chemical potential there faster, leading to a higher charging speed.

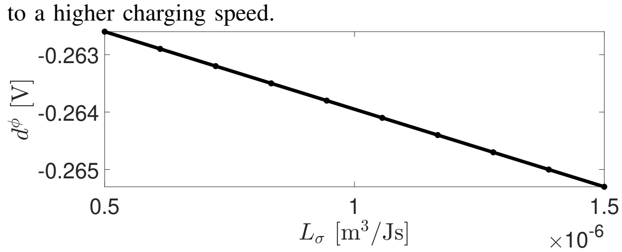

(d) High interfacial mobility intensifies the electric field curvature, indicating a different mechanism of dendrite inhibition than high electrode conductivity.

Fig. 8: The relation between interfacial mobility L_{σ} and different descriptors defined in Table IV.

VI. Conclusion

We introduced a numerically efficient method for optimizing electrodeposition processes with respect to a general objective function using an arbitrary set of parameters. This approach is based on Bayesian optimization and uses a numerical solution of the phase-field partial differential equations over a fixed time interval. This time interval is flexible and can be chosen to optimize the short- or long-term behavior of electrodeposition processes. Using a low-complexity optimization framework, the proposed approach has great potential for controlling various aspects of electrodeposition processes by tuning the right parameters of battery cells.

We used this framework to minimize dendrite growth and maximize charging speed using the following parameters: electrode conductivity, electrolyte conductivity, site density in electrolyte, diffusion coefficient of electrolyte, interfacial mobility, and the electrochemical reaction kinetic coefficient.

The results, summarized in Tables I–III, indicate that dendrite suppression and fast charging are generally conflicting objectives when charging under constant voltage, with the curious exception of one parameter: interfacial mobility. Our results show that increasing interfacial mobility can inhibit dendrite growth effectively, without compromising charging speed. This is realized by an easier release of surface tension and an easier adsorption of ions which reduces the surface roughness and accelerates electrodeposition.

To gain more insight into how different parameters influence the electrodeposition process, we introduced a few simple descriptors by localizing the phase-field model across the electrode/electrolyte interface in an infinitesimal time interval. The reduced model and descriptors reveal the close relation between electric and chemical potential fields, dendrite growth and fast charging, and the chemical parameters of a battery cell. As such, they provide a useful method for evaluating the effects of different parameters on the electrodeposition process without simulating the phase-field model. These tools are considered an initial step toward a physically-inspired computationally-tractable model based on phase-field equations for real-time feedback control systems. This shall be a future direction for further research.

ACKNOWLEDGEMENT

This work was funded by the Göran Gustafsson Foundation and the Knut and Alice Wallenberg Foundation through the Wallenberg Initiative Material Science for Sustainability (WISE) and the Wallenberg AI, Autonomous Systems and Software Program (WASP). The computations were enabled by resources provided by the National Academic Infrastructure for Supercomputing in Sweden (NAISS), partially funded by the Swedish Research Council through grant agreement no. 2022-06725.

REFERENCES

[1] Wang, L., Yao, S., Ying, C., Yao, H. & Yang, J. Numerical simulation of factors in charge of dendrite growth in zinc-nickel single flow batteries. *Electrochimica Acta* **475**, 143622 (2024).

[2] Zhao, Y. *et al.* Simulation for the influence of interface thickness on the dendritic growth of nickel-copper alloy by a phase-field method. *ES Materials & Manufacturing* **2**, 45–50 (2018).

[3] Li, Y. *et al.* Understanding the separator pore size inhibition effect on lithium dendrite via phase-field simulations. *Chinese Chemical Letters* **33**, 3287–3290 (2022).

[4] Shen, X., Zhang, R., Shi, P., Chen, X. & Zhang, Q. How does external pressure shape li dendrites in li metal batteries? *Advanced Energy Materials* **11**, 2003416 (2021).

[5] Gao, L. T. & Guo, Z.-S. Phase field simulation of dendrites morphology evolution in sodium metal batteries. *Journal of Power Sources* **613**, 234961 (2024).

[6] Jeon, J., Yoon, G. H., Vegge, T. & Chang, J. H. Phase-field investigation of lithium electrodeposition at different applied overpotentials and operating temperatures. *ACS applied materials & interfaces* **14**, 15275–15286 (2022).

[7] Andersson, M., Taghavian, H., Hjalmarsson, H., Klass, V. L. & Johansson, M. Informative battery charging: integrating fast charging and optimal experiments. *IFAC-PapersOnLine* **56**, 11160–11166 (2023).

[8] Taghavian, H., Drummond, R. & Johansson, M. When are selector control strategies optimal for constrained monotone systems? *arXiv preprint arXiv:2312.08829* (2023).

[9] Garnett, R. *Bayesian optimization* (Cambridge University Press, 2023).

[10] Lai, J., Zhang, H., Xu, K. & Shi, F. Linking Interfacial Structure and Electrochemical Behaviors of Batteries by High-Resolution Electrocapillarity. *Journal of the American Chemical Society* **146**, 22257–22265 (2024). URL https://pubs.acs.org/doi/10.1021/jacs.4c03791.

[11] Hong, Z. & Viswanathan, V. Phase-field simulations of lithium dendrite growth with open-source software. *ACS Energy Letters* **3**, 1737–1743 (2018).

[12] Chen, L. *et al.* Modulation of dendritic patterns during electrodeposition: A nonlinear phase-field model. *Journal of Power Sources* **300**, 376–385 (2015).

[13] Rickman, J., Barmak, K., Sun, Y. & Zangari, G. Correlation function analysis of electrodeposition kinetics and evolving microstructure. *Electrochimica Acta* **461**, 142663 (2023).

[14] Liang, L. *et al.* Nonlinear phase-field model for electrode-electrolyte interface evolution. *Physical Review E—Statistical, Nonlinear, and Soft Matter Physics* **86**, 051609 (2012).

[15] Ahmad, Z., Hong, Z. & Viswanathan, V. Design rules for liquid crystalline electrolytes for enabling dendrite-free lithium metal batteries. *Proceedings of the National Academy of Sciences* **117**, 26672–26680 (2020).

[16] Berg, H. *Batteries for electric vehicles: materials and electrochemistry* (Cambridge university press, 2015).

[17] González Barrio, R. *Introducción al método de elementos finitos: Con ejemplos en Python/FEniCS aplicados al análisis del desempeño de baterías de litio* (2021).

[18] Jian, Q., Sun, J., Li, H., Guo, Z. & Zhao, T. Phase-field modeling of zinc dendrites growth in aqueous zinc batteries. *International Journal of Heat and Mass Transfer* **223**, 125252 (2024).

[19] Arguello, M. E., Gumulya, M., Derksen, J., Utikar, R. & Calo, V. M. Phase-field modeling of planar interface electrodeposition in lithium-metal batteries. *Journal of Energy Storage* **50**, 104627 (2022).

[20] Xiong, Y., Yan, B., Li, Q., Zhi, C. & Fan, J. Phase field modeling of dendrite growth mechanism of mg and li in electrodeposition. *Journal of Power Sources* **597**, 234162 (2024).

[21] Gao, L. & Guo, Z. Phase-field simulation of li dendrites with multiple parameters influence. *Computational Materials Science* **183**, 109919 (2020).

[22] Ren, Y., Zhou, Y. & Cao, Y. Inhibit of lithium dendrite growth in solid composite electrolyte by phase-field modeling. *The Journal of Physical Chemistry C* **124**, 12195–12204 (2020).

[23] He, H. *et al.* Engineering interfacial layers to enable zn metal anodes for aqueous zinc-ion batteries. *Energy Storage Materials* **43**, 317–336 (2021).

[24] Ding, F. *et al.* Dendrite-free lithium deposition via self-healing electrostatic shield mechanism. *Journal of the American Chemical Society* **135**, 4450–4456 (2013).

[25] Tian, R. *et al.* Quantifying the effect of electronic conductivity on the rate performance of nanocomposite battery electrodes. *ACS Applied Energy Materials* **3**, 2966–2974 (2020).

[26] Yi, T.-F., Wei, T.-T., Li, Y., He, Y.-B. & Wang, Z.-B. Efforts on enhancing the li-ion diffusion coefficient and electronic conductivity of titanate-based anode materials for advanced li-ion batteries. *Energy Storage Materials* **26**, 165–197 (2020).

[27] Rehnlund, D., Ihrfors, C., Maibach, J. & Nyholm, L. Dendrite-free lithium electrode cycling via controlled nucleation in low LiPF6 concentration electrolytes. *Materials Today* **21**, 1010–1018 (2018). URL https://linkinghub.elsevier.com/retrieve/pii/S136970211830467X.

[28] Wang, K., Xiao, Y., Pei, P., Liu, X. & Wang, Y. A phase-field model of dendrite growth of electrodeposited zinc. *Journal of the Electrochemical Society* **166**, D389 (2019).

[29] Xiao, J. How lithium dendrites form in liquid batteries. *Science* **366**, 426–427 (2019). URL https://www.science.org/doi/10.1126/science.aay8672.

[30] Cogswell, D. A. Quantitative phase-field modeling of dendritic electrodeposition. *Physical Review E* **92**, 011301 (2015).

[31] Liu, Y. *et al.* Insight into the critical role of exchange current density on electrodeposition behavior of lithium metal. *Advanced Science* **8**, 2003301 (2021).

[32] Schlesinger, M. *Modern Electroplating*. No. 52 in The ECS series of texts and monographs (Wiley, Hoboken, 2011), 5th ed edn.

[33] Sun, X. *et al.* Revisiting the Electroplating Process for Lithium-Metal Anodes for Lithium-Metal Batteries. *Angewandte Chemie International Edition* **59**, 6665–6674 (2020). URL https://onlinelibrary.wiley.com/doi/10.1002/anie.201912217.

[34] Ding, F. *et al.* Dendrite-Free Lithium Deposition via Self-Healing Electrostatic Shield Mechanism. *Journal of the American Chemical Society* **135**, 4450–4456 (2013). URL https://pubs.acs.org/doi/10.1021/ja312241y.

[35] Wang, J. *et al.* Toward Dendrite-Free Metallic Lithium Anodes: From Structural Design to Optimal Electrochemical Diffusion Kinetics. *ACS Nano* **16**, 17729–17760 (2022). URL https://pubs.acs.org/doi/10.1021/acsnano.2c08480.

[36] phase-field simulation and other examples with python/fenics. https://sourceforge.net/projects/python-fenics-examples. Accessed: 2024-06-04.

[37] Related repositories in https://github.com/taghavian-c.

Appendix

A. Implementation details

We remark the details about the hardware and software used for this study in this section. The two-point boundary value problem (15) was solved using the four-stage Lobatto IIIa collocation formula by the Matlab built-in function bvp5c. The system of partial differential equations (1)-(3) was numerically solved using the finite element method, by the Fenics software. We built upon the work [36] for this purpose. To solve the Bayesian optimization problem (12), we used the Ax-BoTorch platform with the qlogNEI acquisition function and Matern 5/2 kernel in all experiments. The number of trials used for each of the first experiments in Section IV-A was 20, for the second experiment of Section IV-A was 100, and for each experiment in Section IV-B was 20. Solving the Bayesian optimization problems and simulating the complete phase-field models were carried out on the Tetralith supercomputer at NSC with 32 cores. The second experiment of Section IV-A took 24 hours 13 minutes and 17 seconds to complete and the simulation performed in Section IV-C took 5 days, 4 hours, 47 minutes, and 1 second to complete on this machine. All the codes will be accessible in [37] after acceptance.